(Received 10 July 2024, Accepted 19 September 2024, Scheduled 2 November 2024)

Modeling the Compression of Modulated Electromagnetic Pulses in a Straight Waveguiding Defect of Two-Dimensional Photonic Crystal

Vadym Pazynin[1], Kostyantyn Sirenko[2,*], Maksym Maiboroda[2], Miramgul Tokasheva[3], Akbota Tolegenova[3], and Wilhelm Keusgen[1]

[1] *Technical University of Berlin, Berlin, Germany*
[2] *O. Ya. Usikov Institute for Radiophysics and Electronics, National Academy of Sciences of Ukraine, Kharkiv, Ukraine*
[3] *L. N. Gumilyov Eurasian National University, Astana, Kazakhstan*

ABSTRACT: The paper presents the results of numerical modeling of the compression of a frequency-modulated electromagnetic pulse in a straight waveguiding defect of a finite two-dimensional photonic crystal. For the first time, the time reversal method was used to accurately compute the temporal profile of a current pulse that excites an electromagnetic wave that is being compressed in such a structure, given that its temporal profile (electric field intensity) has a specified shape at a given point in space. The photonic crystal consists of an array of sapphire bars with a square cross-section of 1 mm × 1 mm, arranged in free space at a distance of 1 mm from each other. In this model, the boundaries of the frequency range containing the crystal's band gap (from 35.6 to 46.5 GHz), the optimal width of the waveguiding defect (4 mm), and the shape of the excitation current pulse for the waveguiding defect with a length of 0.5 m were found. The obtained pulsed power amplification coefficient is approximately 7.48. A photonic-crystal analog of an H-plane horn antenna was used to radiate the compressed pulse into free space.

1. INTRODUCTION

Increasing power, reducing duration, and shifting operational ranges towards higher frequencies are among the main trends in the development of modern electromagnetic pulse (EMP) technologies. One possible way to address these challenges is to use the dispersion compression of long modulated pulses in waveguides with group velocity dispersion. If in a waveguide, the Fourier components of a pulse propagate with different velocities, it is possible to adjust the timing of their movement (or, in other words, the frequency modulation of an input pulse) so that their peaks arrive simultaneously at the output. As a result, there is a localized in space and time increase of the amplitude and power of EMP (so-called spatio-temporal focusing [1]). Simultaneously, in accordance with the energy conservation law, the pulse's duration is shortened. This process of the dispersion compression is a generalization of the matched filter technique to systems with distributed parameters [2].

In general, the dispersion element in such a system could be any. In the microwave range, hollow metal waveguides [1, 3], plasma-filled waveguides [4], waveguides with periodic dielectric loading [5, 6], waveguides with corrugated walls [7–11], and waveguides with reflectionless cavity chains [12] have been used. The pulsed power amplification coefficients reported in these works are between 10 and 20, and the bandwidth is only a few percent of the central frequency. Since these two parameters are proportional to each other [2], the transition to pulses with a wider frequency band naturally results in greater amplification coefficient values.

The main problem that arises here is the accurate determination of the temporal profiles of input pulses. Typically, the so-called kinematic approximation is used for this purpose [7]. In this approximation, EMP is considered as a set of "particles", each characterized by the dispersion-law-governed frequency and velocity. Knowing the dispersion element's length and the velocity of "particles", the delay time with which each "particle" should enter the dispersion element, i.e., the law of input pulse's frequency modulation, is determined. The kinematic approximation yields relatively small errors for narrowband pulses, which allows their effective compression [7–11]. However, for wideband pulses (for example, pulses with the spectrum width of one octave), it leads to prohibitively large errors, even in the case of such simple dispersion elements as segments of hollow regular waveguides [13].

An alternative to the kinematic approximation is the time reversal method (TRM), which allows determining the temporal profile of input pulses regardless of the width of their spectrums and the type of dispersion elements [14–20]. This method is based on the possibility to change the sign of the time variable in the Maxwell's equations and allows to reconstruct the evolution of an impulse wave before it arrives at a given point in space with a specified temporal profile. In particular, this method could be used to accurately reconstruct the temporal profile of EMP at the input of a dispersion element. TRM has demonstrated its effectiveness in modeling the dispersion com-

* Corresponding author: Kostyantyn Sirenko (k.sirenko@gmail.com).

pression of EMPs with the spectrum widths of up to several octaves and various waveguiding dispersion elements [21–27]. Additionally, an important advantage of TRM is its capacity for the precise calculations of the temporal profiles of input pulses for lossy dispersion elements [21, 22], even when input and output signals are different physical quantities [24, 26, 27].

In this work, we study the possibility of compressing frequency-modulated EMPs propagating in waveguiding defects of photonic crystals. Photonic crystals are periodic structures in one, two, or three dimensions, and have elementary cells composed of dielectric elements of various geometries [28–31]. The absence of metal parts allows for the construction of devices with unique characteristics in frequency ranges where the use of metal is undesirable or impossible due to high energy losses in the skin layer (for wavelengths shorter than 1 cm). An important feature of photonic crystals is the presence of band gaps, i.e., frequency ranges where wave propagation is impossible. By disrupting the periodicity of photonic crystal (creating a defect), a waveguiding channel (waveguide) is formed for the directional transmission of electromagnetic energy. Such photonic-crystal waveguides also exhibit the dispersion and could be used for the compression of EMPs. This paper presents the mathematical model of a two-dimensional photonic crystal with a waveguiding defect and details the modeling of EMP compression in it.

2. MATHEMATICAL TOOLS

The model under consideration is two-dimensional. This means that the field, its sources, and scatterers do not depend on one of the Cartesian coordinates (the x-coordinate, Fig. 1). E-polarized waves are considered, i.e., waves whose non-zero components are $E_x = E_x(y,z,t)$, $H_y = H_y(y,z,t)$, and $H_z = H_z(y,z,t)$. The following initial-boundary value problem is used to describe transient electromagnetic processes:

$$\begin{cases} \dfrac{\varepsilon}{\eta_0}\dfrac{\partial E_x}{\partial t} = \dfrac{\partial H_z}{\partial y} - \dfrac{\partial H_y}{\partial z} - \sigma E_x - j_x, \\ \eta_0 \dfrac{\partial H_y}{\partial t} = -\dfrac{\partial E_x}{\partial z}, \quad \eta_0 \dfrac{\partial H_z}{\partial t} = \dfrac{\partial E_x}{\partial y}, \\ \quad t \geq 0, \quad g \equiv \{y,z\} \in \mathbf{Q_L}, \\ E_x(g,0) = H_y(g,0) = H_z(g,0) = 0, \\ \partial E_x(g,0)/\partial t = \partial H_y(g,0)/\partial t = \partial H_z(g,0)/\partial t = 0, \\ E_x^{(i)}(g,t)\big|_{g\in\mathbf{B}} = E_x^{(j)}(g,t)\big|_{g\in\mathbf{B}}, \\ H_{tan}^{(i)}(g,t)\big|_{g\in\mathbf{B}} = H_{tan}^{(j)}(g,t)\big|_{g\in\mathbf{B}}, \\ \int\limits_{V_C} (\varepsilon E_x^2 + \mu(H_y^2 + H_z^2))dV < \infty, \\ \mathbf{A_L}\left[E_x(g,t)\right]_{g\in\mathbf{L}} = 0. \end{cases} \tag{1}$$

Here, g represents a point in the Cartesian plane $\{y,z\}$; t is the normalized time, which is the product of the natural time t' and the speed of light in vacuum ($t = ct'$, $c = 299\,792\,458$ m/s) and having dimensions of meters (the SI units are used for other physical quantities); $\varepsilon = \varepsilon(g)$ is the relative dielectric permittivity; $\sigma = \sigma(g)$ is the specific conductivity; $j_x = j_x(g,t)$ is the external current density; $\eta_0 = \sqrt{\mu_0/\varepsilon_0} = \mu_0 c = 376.730\ldots\Omega$ is the impedance of free space; $\mu_0 = 4\pi \times 10^{-7}$ H/m and $\varepsilon_0 \approx 8.854 \cdot 10^{-12}$ F/m are the magnetic and electric constants; $\mathbf{Q_L}$ is the analysis domain, which is a fragment of the Cartesian plane $\{y,z\}$, bounded by the rectangular virtual boundary $\mathbf{L}$, containing all essential sources and scatterers of the field (Fig. 1). The first two lines in (1) are the Maxwell's equations for non-zero field components; the fourth and fifth lines are initial conditions; the sixth and seventh lines are continuity conditions for tangential field components at the boundaries $\mathbf{B}$ of dielectric objects (i, j are the numbers of these objects); the eighth line is conditions on the edges $\mathbf{V}$, i.e., points on the plane $\{y,z\}$ where the boundaries of objects have sharp bends (the requirement of finiteness of energy in any finite volume V_C containing the edge $\mathbf{V}$ [32]); the last line is a formal operator representation of the boundary condition imposed on the field on the virtual boundary $\mathbf{L}$. It is formulated as the solution of the following four auxiliary initial-boundary value problems on each straight segment of $\mathbf{L}$ for auxiliary functions $V_y = V_y(z,t,\varphi;y_i)$ and $V_z = V_z(y,t,\varphi;z_i)$ (y_i, z_i are parameters defining the straight segment of $\mathbf{L}$ where the corresponding auxiliary function is defined):

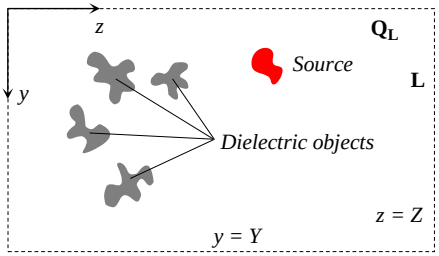

FIGURE 1. Geometry of problems under study. Shapes and quantity of dielectric scatterers could be arbitrary.

$$\begin{cases} E_x(y,z_i,t) = -\dfrac{2}{\pi}\int\limits_0^{\pi/2} \dfrac{\partial V_z}{\partial t} d\varphi, \\ \dfrac{\partial^2 V_z}{\partial t^2} - \sin^2\varphi \dfrac{\partial^2 V_z}{\partial y^2} = \pm \dfrac{\partial E_x}{\partial z}, \quad \begin{Bmatrix} z_i = Z \\ z_i = 0 \end{Bmatrix}, \\ V_z\big|_{t=0} = \partial V_z/\partial t\big|_{t=0} = 0 \end{cases} \tag{2}$$

$$\begin{cases} E_x(y_i,z,t) = -\dfrac{2}{\pi}\int\limits_0^{\pi/2} \dfrac{\partial V_y}{\partial t} d\varphi, \\ \dfrac{\partial^2 V_y}{\partial t^2} - \sin^2\varphi \dfrac{\partial^2 V_y}{\partial z^2} = \pm \dfrac{\partial E_x}{\partial y}, \quad \begin{Bmatrix} y_i = Y \\ y_i = 0 \end{Bmatrix}, \\ V_y\big|_{t=0} = \partial V_y/\partial t\big|_{t=0} = 0. \end{cases} \tag{3}$$

At the corner points of the boundary $\mathbf{L}$, functions V_y and V_z are matched by the equations

$$\begin{cases} \dfrac{\partial V_z}{\partial t} + \sin\varphi \dfrac{\partial V_z}{\partial y} = \mp \int\limits_0^{\pi/2} R(\varphi,\varphi') \dfrac{\partial V_y}{\partial z} d\varphi' \quad \begin{Bmatrix} z_i = Z \\ z_i = 0 \end{Bmatrix}, \\ \dfrac{\partial V_y}{\partial t} + \sin\varphi \dfrac{\partial V_y}{\partial z} = \mp \int\limits_0^{\pi/2} R(\varphi,\varphi') \dfrac{\partial V_z}{\partial y} d\varphi' \quad \begin{Bmatrix} y_i = Y \\ y_i = 0 \end{Bmatrix}, \end{cases} \tag{4}$$

where

$$R(\varphi,\varphi') = \frac{\sin^2\varphi'}{\sin^2\varphi + \sin^2\varphi' \cos^2\varphi}. \tag{5}$$

The relations (2)–(5) represent exact absorbing boundary conditions, which are the basis of the exact absorbing conditions (EAC) method [33–39]. They are rigorously derived from the Maxwell's equations and accurately describe waves leaving the analysis domain through the virtual boundary with EAC imposed. When solving initial-boundary value problems numerically, this feature allows to reduce the level of waves reflected from the virtual boundary to a level below the error of numerical method in use in all points of the analysis domain. This ability of EAC to correctly and unlimitedly "absorb" the waves incident on the virtual boundaries is their advantage over the widely used Perfectly Matched Layer (PML) technique [39]. In particular, the EAC method enables accurate time-domain modeling of wave processes in open resonant structures with eigen oscillations having a quality factor that can exceed 10^7 [40]. In this case, the time of interaction of outgoing waves with the virtual boundaries can be more than 10^6 periods of the working oscillation, and the resulting solution does not display the presence of waves reflected from the virtual boundaries.

The shape, quantity, and arrangement of dielectric objects comprising the structures under study (photonic crystals) could be arbitrary and should be set when formulating initial-boundary value problems. In this paper, two-dimensional crystals made of sapphire bars with square cross-sections are considered. The field source is a current filament with the density $j_x(t)$. The time dependence of $j_x(t)$ could be arbitrary (with some insignificant constraints) and is set depending on the specifics of each particular numerical experiment.

The initial-boundary value problem (1)–(5) is resolved using the Finite-Difference Time-Domain (FDTD) method [41]. This method is efficient, relatively straightforward to implement, and allows solving two-dimensional initial-boundary value problems using widely-available personal computers. The numerical solution to the problem (1)–(5) is the values of grid functions corresponding to the field components $E_x(g,t)$, $H_y(g,t)$, and $H_z(g,t)$ at all nodes of the computational grid. If necessary, the time-domain data is converted into frequency characteristics using standard Fourier transform

$$\widetilde{u}(k) \;=\; FT\left[u(t)\right] = \frac{1}{2\pi}\int_{-\infty}^{\infty} u(t)e^{ikt}dt, \qquad (6)$$

$$u(t) \;=\; FT^{-1}\left[\widetilde{u}(k)\right] = \int_{-\infty}^{\infty} \widetilde{u}(k)e^{-ikt}dk. \qquad (7)$$

Here, $k = 2\pi/\lambda$ is the wavenumber; $\lambda = c/f$ is the wavelength in free space; f is the linear frequency.

3. PHOTONIC CRYSTAL

Let us consider a finite photonic crystal in the form of an array of sapphire bars oriented along the x axis and having square cross-section in the $\{y,z\}$ plane, Fig. 2(a). The cross-section size of each bar is 1 mm × 1 mm, the distance between them is 1 mm in each coordinate direction. The relative dielectric permittivity of sapphire is $\varepsilon = 11.6$ [42–44], and we neglect dielectric losses at this stage. The crystal's size is set to 28×28 bars or 55 mm × 55 mm.

Let us determine frequency parameters of the crystal's band gap [45, 46]. To do this, the four bars are removed from the central part of the crystal (Fig. 2(a)), and a current filament is placed at the geometric center of the crystal (point S). The current density is set by the function

$$j_x(t) \;=\; 4S(t)\cos\big(k_c(t-T)\big)\frac{\sin\big(k_s(t-T)\big)}{t-T}, \qquad (8)$$

$$S \;=\; x^2(3-2x),\; x(t) = \begin{cases} \frac{t-t_0}{T-t_0}, & t_0 \le t \le T \\ \frac{t-t_1}{T-t_1}, & T \le t \le t_1 \\ 0, & t < 0,\; t > t_1 \end{cases} \qquad (9)$$

with $A = 4$, $k_c = k_s = 600\,\mathrm{m}^{-1}$, $t_0 = 0$ m, $t_1 = 1$ m, and $T = (t_0 + t_1)/2$. The amplitude spectrum of this pulse (Fig. 2(b)) has approximately unit value in the range $0 < k < 1\,200\,\mathrm{m}^{-1}$ ($0 < f < 57.2$ GHz). To record the field passing through the crystal, we set five observation points P_1, P_2, …, P_5, at a distance 10 mm from the crystal (from the nearest row of bars). The distance between adjacent observation points is 6.75 mm, which is approximately $1/8$ of the crystal's width. Exciting the crystal with the pulse (8) allows us to determine the fields $E_x(t)|_{P_i}$ at the observation points P_i, as well as their

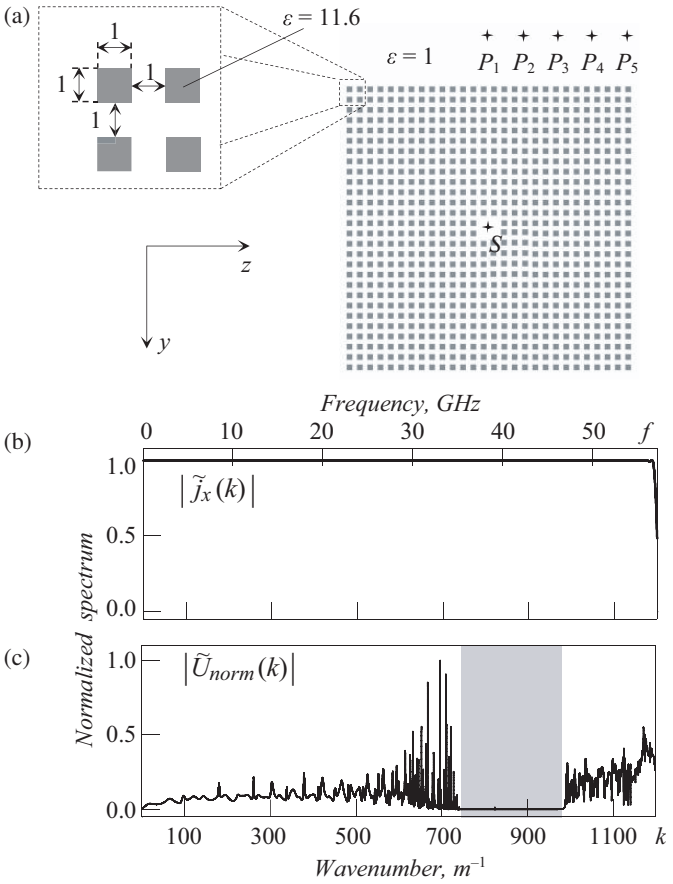

FIGURE 2. (a) General view of finite photonic crystal with defect in central part containing the excitation current filament S. (b) Excitation pulse spectrum. (c) Normalized aggregated spectrum at the observation points P_1–P_5. Dimensions of the crystal's unit cell are in millimeters, the crystal size is 55 mm × 55 mm.

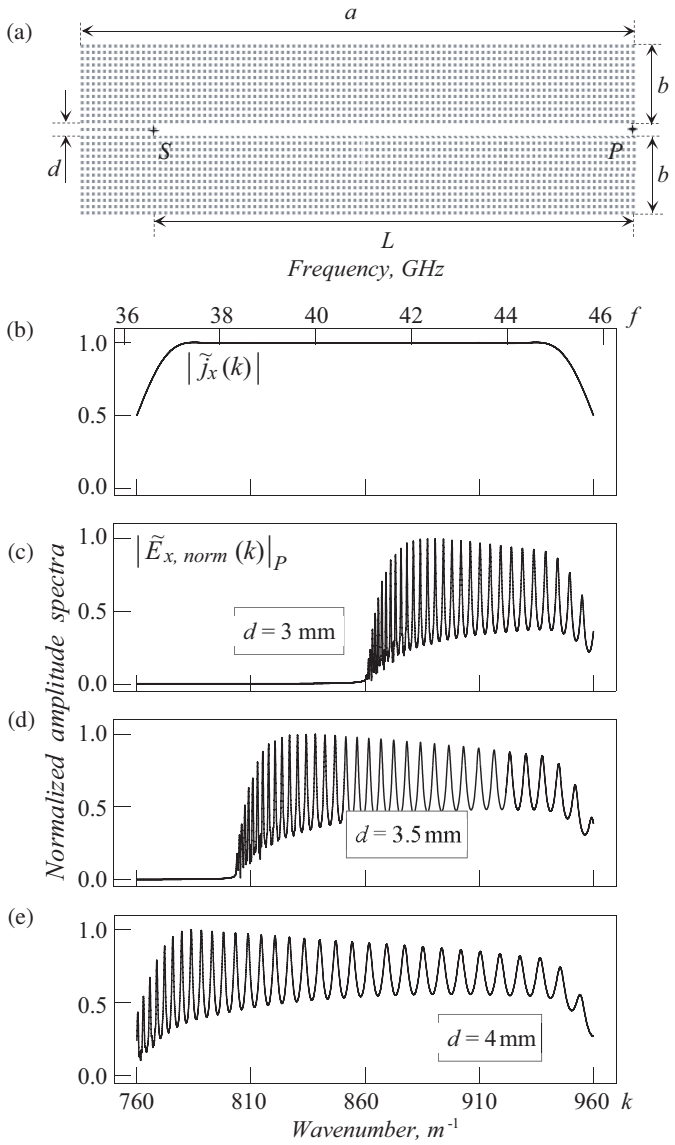

FIGURE 3. (a) General view of finite photonic crystal with waveguiding defect. (b) Amplitude spectrum of the excitation pulse, the current filament is located at the point S. Normalized amplitude spectra of the field at the observation point P for (c) $d = 3\,\text{mm}$, (d) $d = 3.5\,\text{mm}$, and (e) $d = 4\,\text{mm}$.

spectra $\widetilde{E}_x(k)|_{P_i}$. These spectral functions are summed and normalized as

$$\widetilde{U}(k) = \sum_i \left|\widetilde{E}_x(k)\right|_{P_i}, \quad \widetilde{U}_{norm}(k) = \frac{\widetilde{U}(k)}{\max \widetilde{U}(k)}. \qquad (10)$$

The function $\widetilde{U}_{norm}(k)$ allows to assess the crystal's band gaps because it contains aggregate information from multiple observation points, and the possible absence of certain spectral components of the field at one point may be compensated by their presence at others. On the other hand, the absence of specific frequency components simultaneously at all observation points indicates complete opacity of the crystal at the corresponding frequencies. Fig. 2(c) illustrates this, in which the frequency band where the function $\widetilde{U}_{norm}(k)$ is practically zero is shaded in gray. This represents the photonic crystal's band gap, and its boundaries can be approximately determined as

$$746 < k < 975\,\text{m}^{-1} \text{ or } 35.594 < f < 46.521\,\text{GHz}. \qquad (11)$$

In the same time, in the narrow vicinity of the wavenumber $k = 824.1\,\text{m}^{-1}$, the resonant transmission through the crystal occurs. The level of this transmission and the frequency band where this effect is observed are quite small and do not affect the results of numerical experiments.

Now, to enable a directed energy transmission inside the crystal, it is necessary to create an extended defect in the crystal's structure. The simplest way to achieve this is to remove one row of the bars. However, the bars removal alone is insufficient to create a waveguiding channel with frequency characteristics required for our purposes. The crystal's band gap must entirely overlap with the frequency band where the waveguiding channel supports wave propagation, only in this case it is possible to effectively utilize the entire frequency range occupied by the band gap. Additionally, by an analogy with a hollow metal waveguide, the band gap is required to be as close as possible to the cutoff frequency of the waveguiding channel. In this scenario, its dispersion properties will be most pronounced, and the difference between maximum and minimum values of the group velocity in the operating frequency range will be maximal. Since determining the cutoff frequency analytically is very difficult, we do it numerically [45, 46].

To achieve this, the geometry of the photonic crystal is modified as shown in Fig. 3(a). Now it is composed of two blocks of 100×13 sapphire bars ($a \times b = 199\,\text{mm} \times 25\,\text{mm}$). A defect is created between these blocks by removing 87 (out of 100) bars from one row. The remaining 13 bars enclose the waveguiding defect on one side, and their centers lie on the symmetry plane of the crystal. The length of this waveguiding defect is $L = 174\,\text{mm}$. Its width d can vary within a certain range, and it is chosen in accordance with the requirements outlined in the previous paragraph. A current filament is placed at the point S, which coincides with the center of the first removed bar (the 14-th bar in the row). The observation point P is located at the geometric center of the last removed bar (the 100-th bar in the row). Exciting the structure with the pulse (8) with $A = 4$, $k_c = 860\,\text{m}^{-1}$, $k_s = 100\,\text{m}^{-1}$, $t_0 = 0\,\text{m}$, $t_1 = 0.5\,\text{m}$ (its spectrum is shown in Fig. 3(b)) allows us to find the amplitude spectrum of the wave at the observation point P and estimate the optimal value of the width d.

Figures 3(c), 3(d), and 3(e) plot the normalized spectra $|\widetilde{E}_{x,norm}(k)|_P$ for various values of d. It is evident that, similar to hollow metal waveguides, there is a frequency range where the crystal's waveguiding channel does not support wave propagation, and as d increases, the upper bound of this range shifts towards lower frequencies. The value $d = 4\,\text{mm}$ provides the most suitable combination of the cutoff frequency of such a waveguide and the band gap of the crystal, so it is chosen for further numerical experiments.

4. TIME REVERSAL METHOD

Let us modify the crystal geometry again for more efficient pulse compression and radiation into free space, see Fig. 4.

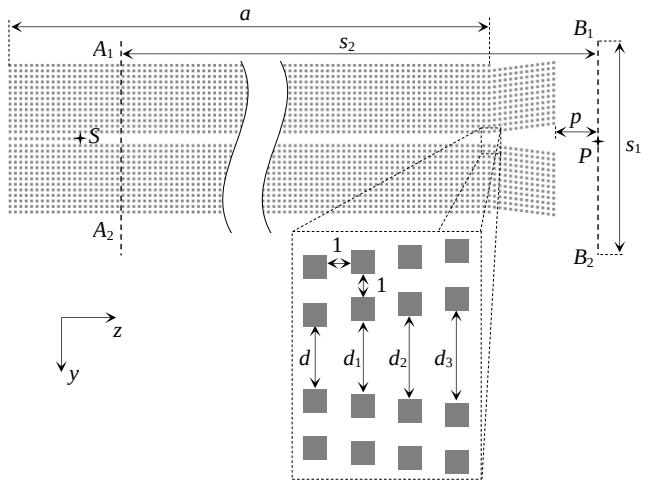

FIGURE 4. General view of photonic crystal with waveguiding defect and matching section for efficient radiation of compressed pulses into free space.

First, the length of the main part of the crystal is increased to 499 mm (250 sapphire bars). This allows achieving a higher pulse compression ratio than in a shorter section of the waveguiding channel. Second, dielectric losses are added to our model: for the dielectric loss tangent $\tan\delta = 10^{-4}$ and wavenumber $k = 860\,\mathrm{m}^{-1}$ (the middle of operating frequency range), the specific conductivity of the sapphire bars is $\sigma = ck\varepsilon\varepsilon_0 \cdot \tan\delta = 2.64 \cdot 10^{-3}$ S/m. Third, a matching section is added to the main part of the crystal, and it has the form of a smooth expansion of the waveguiding channel (a photonic-crystal analogue of an H-plane horn). The need for such a section is due to the presence of oscillations in the spectral characteristics shown in Figs. 3(c)–(e), indicating a relatively high level of wave reflection from the open end of the waveguiding channel and the formation of a resonance volume inside it. This is an undesirable effect whose contribution should be reduced as much as possible before conducting the EMP compression experiment.

The matching section is constructed from two symmetrical blocks, consisting of 12 columns with 12 sapphire bars in each. Distances (along the coordinate directions) between all neighboring bars in the section, just like in the main crystal, are 1 mm. The distance between the nearest bars of the main crystal and the bars of the matching section is also 1 mm. When moving along the waveguiding channel inside the matching section towards free space, the distances between the nearest bars on both sides of the channel increase by 0.5 mm: $d = 4$ mm, $d_1 = 4.5$ mm, $d_2 = 5$ mm, $d_3 = 5.5$ mm, and so on till $d_{12} = 10$ mm.

Let us use now the described photonic crystal model (Fig. 4) to simulate the compression of EMP. To determine the temporal profile of the current exciting the pulse to be compressed, TRM is employed. According to this method, the following steps need to be executed:

1. Specifying the temporal profile of the objective pulse $u^{obj}(t)$, which is (desired) to be obtained at a specified point in space.
2. Excitation of the dispersive waveguiding structure by the pulse $u^{obj}(t)$ and calculation of the temporal profile of the pulse $u^{tran}(t)$ at the observation point.
3. Extraction of the essential part of $u^{tran}(t)$, its inversion in time. The result of this step is the pulse $u^{rev}(t)$.
4. Finding the frequency-dependent factor ξ which determines the signal's losses as it propagates from the excitation point to the observation point.
5. Multiplication of spectral components of the function $u^{rev}(t)$ by ξ^2 and obtaining the desired temporal profile of the input signal, $u^{src}(t)$.
6. Excitation of the dispersion structure by the signal $u^{src}(t)$ and simulation of the compression of the induced EMP.

Below are the results obtained executing these six steps. The current filament serving as the excitation source is located at the point S. The observation point P is located in free space at the distance $p = 9$ mm from the radiator's aperture in the crystal's plane of symmetry.

Step 1. The temporal profile of the objective pulse $u^{obj}(t)$ is defined by the function (8) with $A = 4$, $k_c = 855\,\mathrm{m}^{-1}$, $k_s = 75\,\mathrm{m}^{-1}$, $t_0 = 0$ m, $t_1 = 2T = 0.35$ m, see Fig. 5(a). Such parameters selection allows to localize the spectrum of this pulse $\left|\widetilde{u}^{obj}(k)\right|$ (Fig. 5(b)) within the crystal's band gap (11). At the points $k = 750\,\mathrm{m}^{-1}$ and $k = 960\,\mathrm{m}^{-1}$, which can be regarded as approximate boundaries of the frequency range occupied by the signal u^{obj}, the function $|\widetilde{u}^{obj}(k)| < 10^{-2}$ ($|\widetilde{u}^{obj}(k)| \approx 0.004$ at these points).

Step 2. Figure 5(c) plots the computed time dependence of the electric field $E_x^{tran}(t)|_P$ at the point P, induced by the current pulse with the density $j_x(t) = u^{obj}(t)$ placed at the point S (1 mm × 1 mm area occupied by the first removed sapphire bar from the waveguiding channel). Its normalized amplitude spectrum $|\widetilde{E}^{tran}_{x,norm}(k)|_P$ is plotted in Fig. 5(d), black line, left axis.

Step 3. A significant portion of $E_x^{tran}(t)|_P$ has a smooth envelope at the times $0.95 < t < 2.95$ m (this time interval is outlined by dashed lines in Fig. 5(c)). The lower bound of this time range corresponds to the arrival time at the observation point of frequency components of the pulse propagating in the crystal's defect with maximum group velocity. It can be shown that the value of this velocity falls within the range of 0.54 to 0.67 times the speed of light in vacuum. This uncertainty is related to the uncertainty in defining the moment when these components start propagating along the crystal's defect. The value 0.54 is obtained assuming that this moment coincides with the onset of the pulse $u^{obj}(t)$, which occurs at $t = 0$, while the value 0.67 corresponds to the moment $t = T$, i.e., the maximum of the function $u^{obj}(t)$. The boundary $t = 2.95$ m is also the arrival time at the observation point of the fastest frequency components of the pulse after their passage along the waveguiding defect, partial reflection from the matching section, return to the beginning of the waveguiding channel, reflection from it, and subsequent passage along the waveguiding defect, matching section, and segment of free space to the observation point. Significant here is the time of the wave reflection from

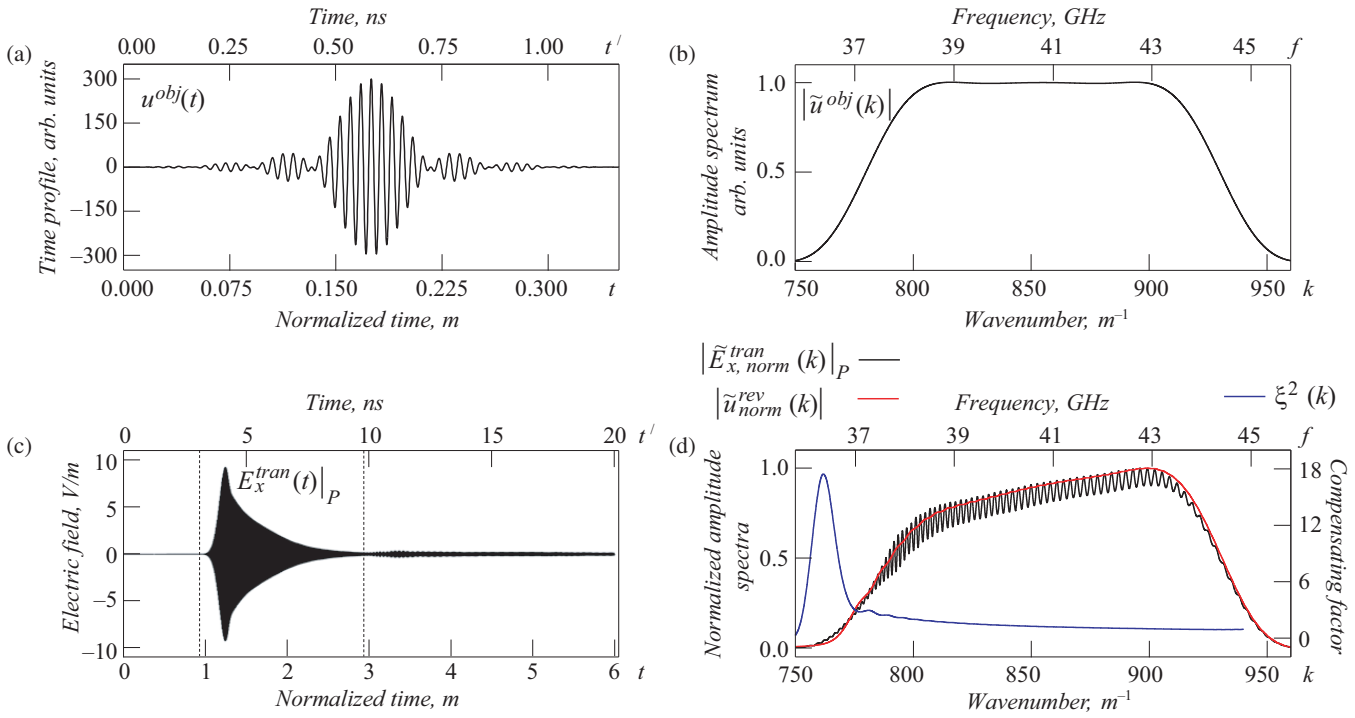

FIGURE 5. (a) Time dependence of the objective pulse $u^{obj}(t)$ and (b) its amplitude spectrum $|\widetilde{u}^{obj}(k)|$. (c) Time dependence of electric field component at the point P, which is induced by the current with density $j_x(t) = u^{obj}(t)$ placed at the point S. (d) Normalized amplitude spectrum of electric field component $|\widetilde{E}^{tran}_{x,norm}(k)|_P$ at the point P (black line, left axis), spectrum of the truncated fragment of this dependence $|\widetilde{u}^{rev}_{norm}(k)|$ (red line, left axis), and the compensating factor $\xi^2(k)$ (blue line, right axis).

the closed part of the waveguiding channel, which ranges from 0.16 m to 0.52 m depending on the identification of the moment when these pulse components start propagating. Due to imperfect matching provided by the matching section, the level of such a wave, having passed through the waveguiding channel three times, is sufficiently high to disrupt the monotonic nature of the envelope of EMP radiated into free space at $t > 2.95$. The function $u^{rev}(t) = E_x^{tran}(2.95 - t)|_P$ for $0 < t < 2$ m.

Step 4. The normalized amplitude spectrum $|\widetilde{u}^{rev}_{norm}(k)|$ is plotted in Fig. 5(d), red line, left axis. Truncating a portion of the pulse $E_x^{tran}(t)|_P$ with a non-monotonic envelope for $t > 2.95$ m has eliminated oscillations in this spectral dependency (compared with $|\widetilde{E}^{tran}_{x,norm}(k)|_P$). The function

$$\xi(k) = \frac{\left|\widetilde{u}^{obj}(k)\right|}{\left|\widetilde{u}^{rev}_{norm}(k)\right|} \tag{12}$$

defines losses incurred by the pulse during a single passage through the dispersion channel between the source and observation points. These losses decrease monotonically with increasing frequency and are not associated with electrical losses in the sapphire bars, but rather with the radiation resistance of the current filament. Similar to hollow metallic waveguides [24], the efficiency of converting energy from a current source localized within photonic crystal into energy of the radiated wave depends on the frequency and increases with its growth.

Step 5. To define losses incurred during the signal's passage from the excitation point to the observation point twice, $\xi(k)$ provided by (12) is squared (Fig. 5(d), blue line, right axis). This quantity allows for the calculation of the temporal profile of the field source through the function $u^{rev}(t)$:

$$j_x(t) \equiv u^{src}(t) = FT^{-1}\left[\xi^2(k) \cdot FT\left[u^{rev}(t)\right]\right] \tag{13}$$

where $FT[\ldots]$ and $FT^{-1}[\ldots]$ are direct (6) and inverse (7) Fourier transforms. The plot of its time dependence is shown in Fig. 6(a), black line, left axis. Additionally, Fig. 6(a) (red line, right axis) plots the frequency modulation law $k(t)$ of the pulse $j_x(t)$:

$$j_x(t) = A(t)\sin\left(\varphi_0 + \int_0^t k(\tau)d\tau\right). \tag{14}$$

Here, $A(t)$ represents the envelope; φ_0 denotes the initial phase; and $k(t)$ is the instantaneous frequency [47]. The normalized amplitude spectrum $|\widetilde{j}_{x,norm}(k)|$ of the function (14) is plotted in Fig. 6(b).

Step 6. Fig. 6(c) plots the computed temporal profile $E_x^{compr}(t)|_P$ of the (compressed) electric field pulse at the observation point P, which is excited by the current (13) located at the point S (see Fig. 4). Fig. 6(d) plots its normalized amplitude spectrum $|\widetilde{E}^{compr}_{x,norm}(k)|_P$. The function $E_x^{compr}(t)|_P$ corresponds to the function $u^{obj}(t)$ up to multiplication by a constant, time shift, and minor deviations associated with the truncation of $E_x^{tran}(t)|_P$ for $t > 2.95$ m,

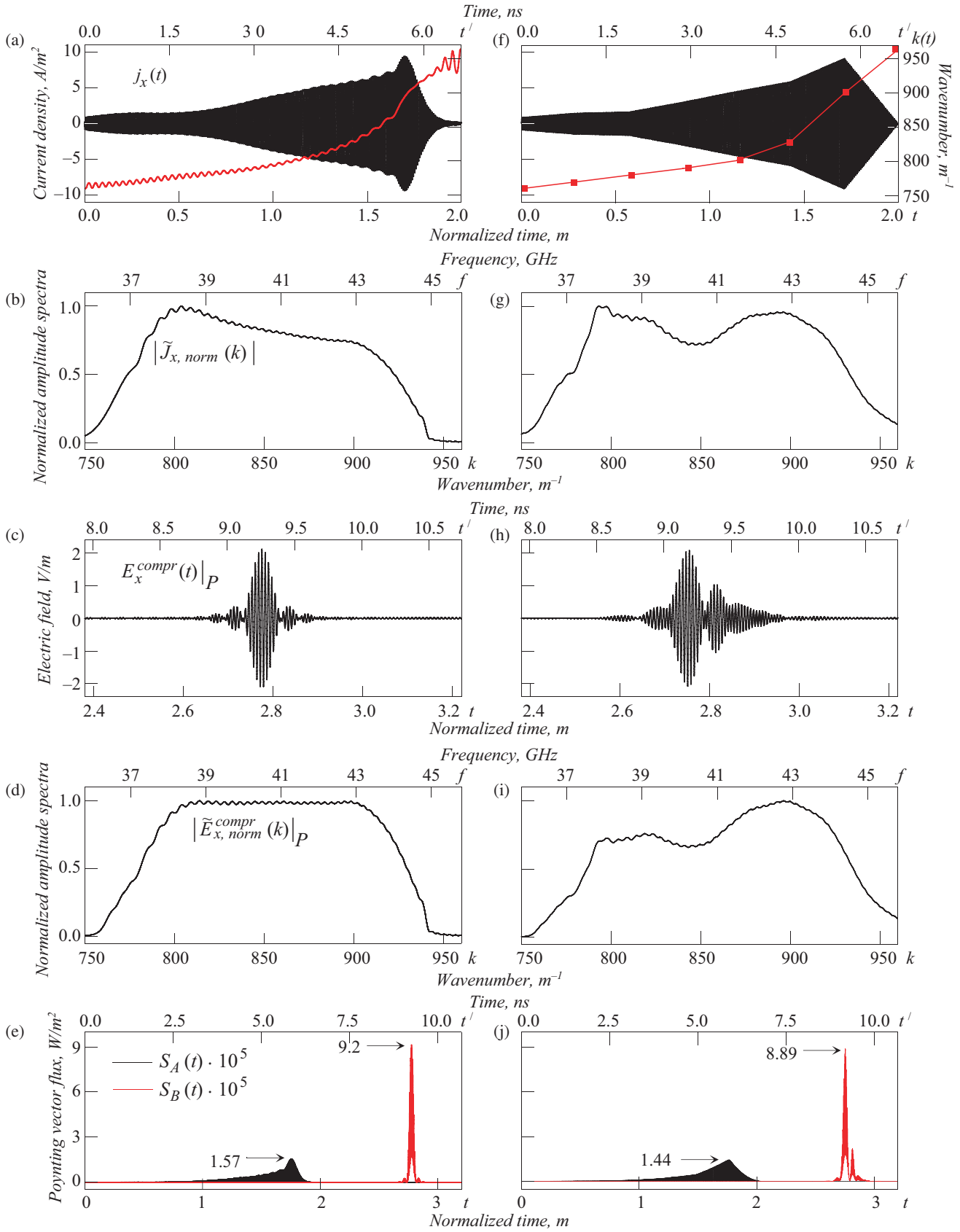

FIGURE 6. (a) Time dependence of external current density $j_x(t)$, which is computed using TRM (black line, left axis), and its frequency modulation law $k(t)$ (red line, right axis). (b) Normalized amplitude spectrum $|\widetilde{j}_{x,norm}(k)|$. (c) Time dependence and (d) normalized amplitude spectrum of electric field component at the point P (compressed pulse). (e) Poynting vector flux through the surfaces A_1A_2 (black line) and B_1B_2 (red line), which are shown in Fig. 4. The right column (subpanels (f)–(j)) plots the same characteristics but for the excitation pulse whose modulation laws are approximated by seven linear segments.

which was done at Step 3. This truncation also accounts for the slight discrepancies between the spectral characteristics $|\widetilde{E}^{compr}_{x,norm}(k)|_P$ and $|\widetilde{u}^{obj}(k)|$. Thus, the numerical experiment on modeling the EMP compression could be considered as successful.

Now, let us assess energy characteristics of the compression process. Direct estimation is challenging because the input pulse is defined as the time dependence of the excitation current (Fig. 6(a), black line, left axis), while the output is represented by the time dependence of the electric field at a fixed point in space (Fig. 6(c)). Converting these physical quantities directly into the energy of electromagnetic field (in vicinities of the corresponding points in space) would not allow a correct assessment of the radiated pulse's power due to the localized nature of these characteristics. This obstacle can be overcome by calculating the fluxes of the Poynting vector of the pulse before and after compression through surfaces lying along the path of propagation of the wave packet being compressed (in longitudinal direction).

To achieve this, we introduce two flat virtual surfaces A_1A_2 and B_1B_2, perpendicular to the axis z. They are shown by the dashed lines in Fig. 4, and the surface B_1B_2 contains the observation point P. Their sizes are $s_1 = 58\,\text{mm}$, and the distance between them is $s_2 = 483\,\text{mm}$. The calculated time dependencies of the Poynting vector fluxes $S_A(t)$ and $S_B(t)$ through these surfaces are plotted in Fig. 6(e). The total energy passing through these two surfaces is

$$E_A \approx \int_0^{3.25} S_A(t)dt \approx 2.24 \cdot 10^{-6} J \tag{15}$$

and

$$E_B \approx \int_0^{3.25} S_B(t)dt \approx 2.15 \cdot 10^{-6} J. \tag{16}$$

Their ratio provides an estimate for the efficiency of compression process. That is, approximately 4% of the energy is lost, partially due to reflection from the matching section (this fraction of energy does not fall within the integration interval $0 \le t \le 3.25\,\text{mm}$) and partially due to lateral radiation, which does not pass through the surface B_1B_2.

In what follows, we consider the pulse passed through the surface A_1A_2 as the input and the pulse passed through the surface B_1B_2 as the output. To estimate the amplification and compression coefficients, it is necessary to establish their temporal boundaries. There is no unique procedure for determining these boundaries, and therefore the durations of these pulses. This poses a certain problem because the pulse's power significantly depends on the time interval over which it is calculated. We set the temporal boundaries for the pulse $S_A(t)$ as $0.11 \le t \le 2.06\,\text{m}$ and for the pulse $S_B(t)$ as $2.65 \le t \le 2.9\,\text{m}$. With these temporal boundaries, the corresponding segments of the pulses $S_A(t)$ and $S_B(t)$ contain $\int_{0.11}^{2.06} S_A(t)dt \approx 2.237 \cdot 10^{-6}\,\text{J}$ and $\int_{2.65}^{2.9} S_B(t)dt \approx 2.146 \cdot 10^{-6}\,\text{J}$ of energy, respectively, which is approximately 0.999 of the values (15) and (16). The following estimates are obtained for the compression coefficient

$$\beta \approx (2.06 - 0.11)/(2.9 - 2.65) = 7.8 \tag{17}$$

and the power amplification coefficient

$$G \approx \frac{2.146 \cdot 10^{-6}}{0.25} \cdot \frac{1.95}{2.237 \cdot 10^{-6}} \approx 7.48 \tag{18}$$

The time dependence of the excitation current's frequency $k(t)$ (Fig. 6(a), red line, right axis) exhibits a non-trivial behavior, which may be uneasy to reproduce in real-world pulse generators. Therefore, it is interesting to explore the potential for linearizing the modulation laws of the excitation pulse. To investigate this possibility, we divide the time interval $0 \le t \le 2\,\text{m}$, where the excitation pulse is defined (Fig. 6(a)), into seven equal subintervals. Within each of these subintervals, the functions $k(t)$ and $A(t)$ are approximated by linear dependencies so that the linearized values of amplitude and frequency coincide with the corresponding values of $k(t)$ and $A(t)$ at the boundaries of these subintervals, which are presented in Table 1.

TABLE 1. Data for interpolating the time profile of external current source.

t, m	A, A/m	k, m^{-1}
0.0000	0.870 170	759.820 481
0.2857	1.461 235	769.735 908
0.5714	1.641 034	779.649 802
0.8571	3.014 393	789.356 950
1.1428	4.522 007	800.892 384
1.4285	5.884 587	828.648 713
1.7142	9.167 814	899.723 164
2.0000	0.000 000	963.916 774

The time dependence of such a linearized current source, created by the data in this table, and its frequency modulation law are plotted in Fig. 6(f), and its normalized amplitude spectrum is plotted in Fig. 6(g). Fig. 6(h), 6(i), and 6(j) demonstrate the results of modeling the compression of EMP excited by such a linearized current source, namely, the pulse at the observation point, its spectrum, and the Poynting vector fluxes through the surfaces A_1A_2 and B_1B_2. All these characteristics differ from those obtained for the pulse with strictly calculated modulation laws $k(t)$ and $A(t)$; however, this difference is not drastic, i.e., small changes of the input (amplitude and frequency) lead to relatively small changes of the output. This is somewhat non-intuitive, as (14) has $k(t)$ inside the integral, and one might expect that approximation errors of $k(t)$ would accumulate during the integration process. However, as the numerical experiment demonstrates, this is not the case. Integrating the obtained Poynting vector fluxes over the same time intervals yields $\int_{0.11}^{2.06} S_A(t)dt \approx 2.74 \cdot 10^{-6}\,\text{J}$ and $\int_{2.65}^{2.9} S_B(t)dt \approx 2.61 \cdot 10^{-6}\,\text{J}$. These values lead to the power amplification coefficient $G \approx 7.43$, which coincides closely with (18).

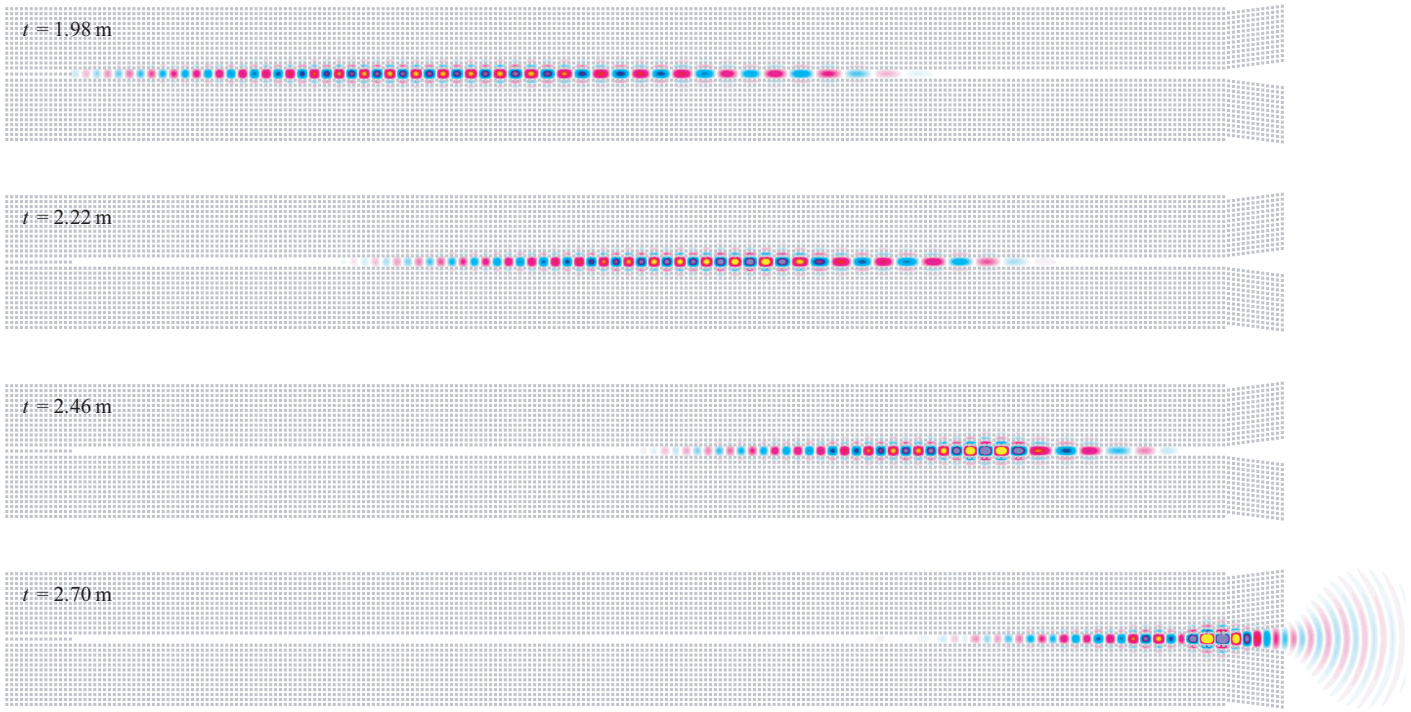

FIGURE 7. Evolution of the pulse being compressed in the photonic crystal's waveguiding defect. E_x field component.

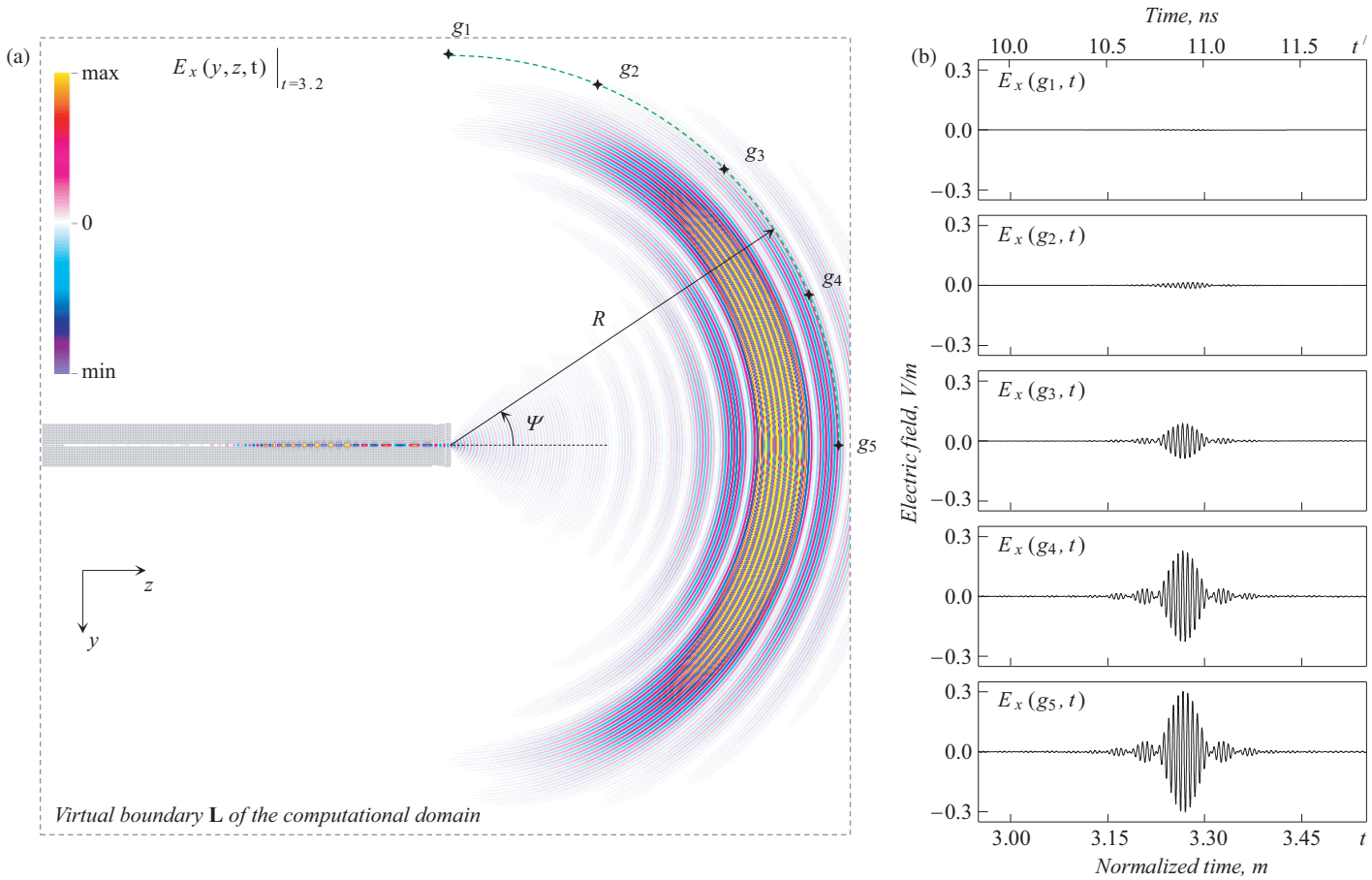

FIGURE 8. Distribution of the electric field component $E_x(y,z)$ in the far zone of the photonic crystal at the time $t = 3.2$ m (a) and time dependences of the E_x component at five observation points $g_1, g_2, \ldots, g_5$ located at a distance $R = 500$ mm (see the green arc) from the open end of the waveguiding defect of the crystal. The angular coordinates Ψ of the observation points are equal to 0, 22.5, 45, 67.5, and 90 degrees.

Dividing the obtained value of G by the dimensionless length of the dispersion channel L_{rel}, where $L_{rel} = (s_2 - p)/d \approx 118$ (see Fig. 4), we obtain an approximate estimate of the power amplification coefficient per unit length equal to a waveguide's transverse size, $G_{rel} = 7.43/118 \approx 0.06$. This approximately coincides with the value of this quantity for a hollow metal waveguide ($G_{rel} \approx 0.09$ for $G \approx 31$ and $L_{rel} \approx 322$ [23]) and is three times smaller than for a flat dielectric waveguide ($G_{rel} \approx 0.19$ for $G \approx 31$, $L_{rel} \approx 165$, and $\varepsilon = 11.5$ [21]). Moreover, the frequency bandwidth occupied by the analyzed pulse (between $k = 750\,\mathrm{m}^{-1}$ and $k = 960\,\mathrm{m}^{-1}$) is approximately one-third of an octave against one octave in [21] and [23], which makes the proposed photonic crystal comparable in dispersion characteristics to "classic" waveguides. Further optimization of the photonic crystal geometry is also possible, aimed at expanding the band gap (see [46, 48]) and minimizing its dimensions by folding the waveguiding defect into a spiral, similar to how it is done in "classic" waveguides [22, 23].

Figure 7 shows the evolution of the considered pulse as it propagates along the waveguiding defect, and the compression could be clearly seen. This sequence of electric field patterns is plotted with an interval $t = 0.24\,\mathrm{m}$ or $t' \approx 0.8\,\mathrm{ns}$.

Figure 8(a) shows the spatial distribution of the electric field component $E_x(y, z)$ of the radiated pulse in the far zone of the photonic crystal aperture at the moment of time $t = 3.2\,\mathrm{m}$. We have placed five observation points at a distance of $R = 500\,\mathrm{mm}$ from the open end of the waveguiding defect of the crystal. They have angular coordinates $\Psi = 0, 22.5, 45, 67.5,$ and 90 degrees. The time dependences of the E_x component at these five points are shown in Fig. 8(b). These spatial and temporal characteristics are close to the corresponding characteristics of such elementary radiators as the open end of a metallic waveguide and a magnetic dipole.

5. CONCLUSION

This work presents the results of numerical modeling of the compression of frequency- and amplitude-modulated EMP in a waveguiding defect of a photonic crystal. The crystal is made of sapphire bars with a square cross-section of 1 mm × 1 mm and a distance of 1 mm between them. The pulse bandwidth (35.79 to 45.80 GHz) approximately coincides with the crystal's band gap (from 35.6 to 46.5 GHz). The time reversal method is used to determine the temporal profile of the excitation current pulse. For the waveguiding channel with a length of approximately 0.5 m, the compression coefficient $\beta \approx 7.8$ and the power amplification coefficient $G \approx 7.48$ were obtained. The possibility of approximating the modulation laws of the excitation current by sequential segments, where the amplitude and frequency have linear time dependence, is investigated. Numerical modeling showed that the approximation of the excitation pulse with a duration of 6.67 ns by seven segments (each with a duration of approximately 0.95 ns) with linear dependence of amplitude and frequency modulations does not lead to any significant change in the energy characteristics of the compression process, although it distorts the shape of the compressed pulse.

The model considered here is two-dimensional. However, it can be easily realized as a real device. For this purpose the entire photonic crystal should be placed between two metal plates lying in the planes $x = const$ (the so-called photonic crystal slab). In this case, all field components of the solutions of the initial-boundary value problems obtained here automatically satisfy the boundary conditions on these planes. This leads to the preservation of the physics of all transient processes in the photonic crystal, and the only possible cause of distortions of the spatial-energetic characteristics of such an object can be either the edges of metal plates or the excitation of higher modes with non-zero indices along the axis perpendicular to the metal plates [49]. It is also obvious that the crystal considered here can be scaled to shorter-wavelength ranges.

ACKNOWLEDGEMENT

The authors acknowledge the financial support by the Federal Ministry of Education and Research of Germany in the program of "Souverän. Digital. Vernetzt." Joint project 6G-RIC, project identification number: 16KISK020K.

REFERENCES

[1] Laflen, J. B. and T. M. Talavage, "A method for delivering spatio-temporally focused energy to a dynamically adjustable target along a waveguiding structure," *IEEE Transactions on Signal Processing*, Vol. 58, No. 3, 1416–1426, Mar. 2010.

[2] Cook, C. E. and M. Bernfeld, *Radar Signals: An Introduction to Theory and Application*, Academic Press, 1967.

[3] Bromley, R. A. and B. E. Callan, "Use of a waveguide dispersive line in an f.m. pulse-compression system," in *Proceedings of the Institution of Electrical Engineers*, Vol. 114, No. 9, 1213–1218, Sep. 1967.

[4] Manheimer, W. M. and B. H. Ripin, "High-power microwave plasma pulse compression," *Physics of Fluids*, Vol. 29, No. 7, 2283–2291, July 1986.

[5] Thirios, E., D. Kaklamani, and N. Uzunoglu, "Pulse compression using a periodically dielectric loaded dispersive waveguide," *Progress In Electromagnetics Research*, Vol. 48, 301–333, 2004.

[6] Thirios, E. C., D. I. Kaklamani, and N. K. Uzunoglu, "Microwave pulse compression using a periodically dielectric loaded dispersive waveguide section," *Electromagnetics*, Vol. 26, No. 5, 345–358, Aug. 2006.

[7] Samsonov, S. V., A. D. R. Phelps, V. L. Bratman, G. Burt, G. G. Denisov, A. W. Cross, K. Ronald, W. He, and H. Yin, "Compression of frequency-modulated pulses using helically corrugated waveguides and its potential for generating multigigawatt RF radiation," *Physical Review Letters*, Vol. 92, No. 11, 118301, Mar. 2004.

[8] Burt, G., S. V. Samsonov, A. D. R. Phelps, V. L. Bratman, K. Ronald, G. G. Denisov, W. He, A. R. Young, A. W. Cross, and I. V. Konoplev, "Microwave pulse compression using a helically corrugated waveguide," *IEEE Transactions on Plasma Science*, Vol. 33, No. 2, 661–667, Apr. 2005.

[9] Zhang, L., S. V. Mishakin, W. He, S. V. Samsonov, M. McStravick, G. G. Denisov, A. W. Cross, V. L. Bratman, C. G. Whyte, C. W. Robertson, *et al.*, "Experimental study of microwave pulse compression using a five-fold helically corrugated waveguide," *IEEE Transactions on Microwave Theory and Techniques*, Vol. 63, No. 3, 1090–1096, Mar. 2015.

[10] MacInnes, P., V. L. Bratman, L. Zhang, G. G. Denisov, W. He, N. G. Kolganov, M. McStravick, S. V. Mishakin, C. W. Robertson, S. V. Samsonov, *et al.*, "Periodic GW level microwave pulses in X-band from a combination of a relativistic backward wave oscillator and a helical waveguide compressor," in *2017 IEEE 21st International Conference on Pulsed Power (PPC)*, 1–4, Brighton, UK, Jun. 2017.

[11] Yurovskiy, L. A., I. V. Zotova, N. S. Ginzburg, M. N. Vilkov, R. M. Rozental, S. V. Samsonov, and E. B. Abubakirov, "Production of multi-gigawatt sub-nanosecond microwave pulses by the method of chirped-pulse-amplification," *IEEE Electron Device Letters*, Vol. 42, No. 3, 426–429, Mar. 2021.

[12] Kuzikov, S. V., "Optimization and synthesis of passive pulse compressors based on reflectionless cavities," *International Journal of Infrared and Millimeter Waves*, Vol. 19, 771–784, May 1998.

[13] Pazynin, V. L., "Compression of frequency-modulated electromagnetic pulses in sections of regular waveguides," *Telecommunications and Radio Engineering*, Vol. 71, No. 20, 1833–1857, 2012.

[14] Laflen, J. B. and T. M. Talavage, "A method for delivering spatio-temporally focused energy to a dynamically adjustable target along a waveguiding structure," *IEEE Transactions on Signal Processing*, Vol. 58, No. 3, 1416–1426, 2010.

[15] Lerosey, G., J. d. Rosny, A. Tourin, A. Derode, G. Montaldo, and M. Fink, "Time reversal of electromagnetic waves," *Physical Review Letters*, Vol. 92, No. 19, 193904, May 2004.

[16] Davy, M., J. De Rosny, J.-C. Joly, and M. Fink, "Focusing and amplification of electromagnetic waves by time reversal in an leaky reverberation chamber," *Comptes Rendus. Physique*, Vol. 11, No. 1, 37–43, 2010.

[17] Hong, S. K., B. T. Taddese, Z. B. Drikas, S. M. Anlage, and T. D. Andreadis, "Focusing an arbitrary RF pulse at a distance using time-reversal techniques," *Journal of Electromagnetic Waves and Applications*, Vol. 27, No. 10, 1262–1275, Jun. 2013.

[18] Hong, S. K., E. Lathrop, V. M. Mendez, and J. Kim, "Ultrashort microwave pulse generation by passive pulse compression in a compact reverberant cavity," *Progress In Electromagnetics Research*, Vol. 153, 113–121, 2015.

[19] Hong, S. K. and H. S. Park, "Ultra-compact pulse compressor for generating ultrawideband short pulses," *Electronics Letters*, Vol. 54, No. 12, 768–770, 2018.

[20] Drikas, Z. B., B. D. Addissie, V. M. Mendez, and S. Raman, "A compact, high-gain, high-power, ultrawideband microwave pulse compressor using time-reversal techniques," *IEEE Transactions on Microwave Theory and Techniques*, Vol. 68, No. 8, 3355–3367, 2020.

[21] Pazynin, V. L. and M. V. Maiboroda, "Compression of electromagnetic pulses in dielectric waveguides of a finite length," *Telecommunications and Radio Engineering*, Vol. 76, No. 14, 1219–1230, 2017.

[22] Maiboroda, M. V., V. L. Pazynin, and H. O. Sliusarenko, "Electromagnetic pulses compression in helically coiled dielectric waveguide," in *2017 XXIInd International Seminar/Workshop on Direct and Inverse Problems of Electromagnetic and Acoustic Wave Theory (DIPED)*, 104–107, Dnipro, Ukraine, Sep. 2017.

[23] Pazynin, V. L. and M. V. Maiboroda, "Electromagnetic pulse compression in sections of helically coiled waveguides," *Telecommunications and Radio Engineering*, Vol. 76, No. 3, 209–225, 2017.

[24] Pazynin, V. L. and M. V. Maiboroda, "Modeling of the compression of wave packets induced by a current filament in a plane-parallel waveguide," *Telecommunications and Radio Engineering*, Vol. 76, No. 16, 1391–1404, 2017.

[25] Pazynin, V. L., V. Z. Mazur, and A. O. Boguslavskaya, "On the feasibility of using a groove waveguide as a dispersive element in a passive microwave power compressor," *Telecommunications and Radio Engineering*, Vol. 77, No. 5, 373–381, 2018.

[26] Pazynin, V. L., "Microwave pulse radiator with passive compression of input signal," *Telecommunications and Radio Engineering*, Vol. 77, No. 1, 13–25, 2018.

[27] Pazynin, V. L. and M. V. Maiboroda, "Compression of electromagnetic pulses in an asymmetric dielectric waveguide," *Telecommunications and Radio Engineering*, Vol. 78, No. 2, 97–107, 2019.

[28] Yasumoto, K., *Electromagnetic Theory and Applications for Photonic Crystal*, Taylor & Francis, 2006.

[29] Joannopoulos, J. D., S. G. Johnson, J. N. Winn, and R. D. Meade, *Photonic Crystals. Molding the Flow of Light*, Princeton University Press, 2008.

[30] Massaro, A., *Photonic Crystals: Introduction, Applications and Theory*, InTech, 2012.

[31] Gong, Q. and X. Hu, *Photonic Crystals. Principles and applications*, CRC Press, 2013.

[32] Mittra, R., *Analytical Techniques in the Theory of Guided Waves*, MacMillan, 1971.

[33] Sirenko, Y. K., S. Ström, and N. P. Yashina, *Modeling and Analysis of Transient Processes in Open Resonant Structures. New Methods and Techniques*, Springer, 2007.

[34] Sirenko, K. and Y. Sirenko, "The exact absorbing conditions method in the analysis of open electrodynamic structures," *Electromagnetic Waves in Complex Systems. Selected Theoretical and Applied Problems*, Chapter 5, 225–326, Springer, 2016.

[35] Sirenko, Y., V. Pazynin, K. Sirenko, and N. Yashina, "Exact absorbing conditions for initial boundary value problems of computational electrodynamics. Review," *A Closer Look at Boundary Value Problems*, Chapter 3, 43–124, Nova Science Publishers, 2020.

[36] Sirenko, Y., "Exact 'absorbing' conditions in outer initial boundary-value problems of the electrodynamics of nonsinusoidal waves. Part 3: Compact inhomogeneities in free space," *Telecommunications and Radio Engineering*, Vol. 59, No. 1&2, 1–31, 2003.

[37] Velychko, L., Y. Sirenko, and O. Velychko, "Time-domain analysis of open resonators. Analytical grounds," *Progress In Electromagnetics Research*, Vol. 61, 1–26, 2006.

[38] Sirenko, K., V. Pazynin, Y. Sirenko, and H. Bagci, "An FFT-accelerated FDTD scheme with exact absorbing conditions for characterizing axially symmetric resonant structures," *Progress In Electromagnetics Research*, Vol. 111, 331–364, 2011.

[39] Pazynin, V. L., S. S. Sautbekov, K. Y. Sirenko, Y. Sirenko, A. A. Vertiy, and N. P. Yashina, "Comparison of exact and approximate absorbing conditions for initial boundary value problems of the electromagnetic theory of gratings," *Telecommunications and Radio Engineering*, Vol. 77, No. 18, 1581–1595, 2018.

[40] Pazynin, V. and W. Keusgen, "Monomode waveguide resonators for microwave and optical applications," in *Proc. of the 2024 IEEE 29th International Seminar/Workshop Direct and Inverse Problems of Electromagnetic and Acoustic Wave Theory (DIPED)*, 7–11, Tbilisi, Georgia, 2024.

[41] Taflove, A. and S. C. Hagness, *Computational Electrodynamics: The Finite-Difference Time-Domain Method*, Artech House, 2000.

[42] Egorov, V. N. and A. S. Volovikov, "Measuring the dielectric permittivity of sapphire at temperatures 93–343 K," *Radiophysics and Quantum Electronics*, Vol. 44, No. 11, 885–891,

2001.

[43] Krupka, J., K. Derzakowski, M. Tobar, J. Hartnett, and R. G. Geyer, "Complex permittivity of some ultralow loss dielectric crystals at cryogenic temperatures," *Measurement Science and Technology*, Vol. 10, No. 5, 387–392, 1999.

[44] Fontanella, J., C. Andeen, and D. Schuele, "Low-frequency dielectric constants of α-quartz, sapphire, MgF_2, and MgO," *Journal of Applied Physics*, Vol. 45, No. 7, 2852–2854, Jul. 1974.

[45] Sirenko, Y., S. Sautbekov, M. Sautbekova, K. Sirenko, H. Sliusarenko, and N. Yashina, "2-D photonic crystals: Rigorous electromagnetic models for infinite, spatially limited and defective structures," *Advances in Materials Science Research*, Vol. 47, Chapter 1, 1–70, Nova Science Publishers, 2021.

[46] Ney, M., K. Sirenko, Y. Sirenko, H. O. Sliusarenko, and N. P. Yashina, "2-D photonic crystals: Electromagnetic models of the method of exact absorbing conditions," *Telecommunications and Radio Engineering*, Vol. 76, No. 3, 185–207, 2017.

[47] Southworth, G. C., "Principles and applications of waveguide transmission," *Bell System Technical Journal*, Vol. 29, No. 3, 295–342, 1950.

[48] Sirenko, Y., K. Sirenko, N. Yashina, and G. Granet, "Synthesis of ultra-wide bandgaps for 2-D photonic crystals of finite thickness," in *Proc. of the International Conference on Antennas and Electromagnetic Systems*, 206–206, Marrakesh, Morocco, 2022.

[49] Andreani, L. C. and D. Gerace, "Photonic-crystal slabs with a triangular lattice of triangular holes investigated using a guided-mode expansion method," *Physical Review B*, Vol. 73, No. 23, 235114, Jun. 2006.